State transfer in a nonlinear cavity magnonic system

Meng-Xia Bi [1], Huawei Fan [1,*], Jun-Ling Che,[1] Ming-Liang Hu [1,†] and Xiao-Hong Yan[2,3]

[1]*School of Science, Xi'an University of Posts and Telecommunications, Xi'an 710121, China*
[2]*College of Electronic and Optical Engineering, Nanjing University of Posts and Telecommunications, Nanjing 210046, China*
[3]*School of Material Science and Engineering, Jiangsu University, Zhenjiang 212013, China*

Nonlinear systems possess complex dynamic behaviors and transition characteristics among various states, which make the behaviors of nonlinear systems hard to predict and control. Here we study state transfer in a nonlinear cavity magnonic system containing the photon and magnon Kerr effects. In this system, the magnon frequency shift exhibits bistability and tristability with coexisting stable states. A given initial state is transferred to one of the coexisting states. Although state transfer is shown from the perspective of the number of excited magnons, which is proportional to the magnon frequency shift, the coexisting state to which the initial state is transferred is determined jointly by the amplitude and phase of the magnon and photon, rather than by the number of excited magnons. Based on the basins of attraction, we explain state transfer and reveal its nonlinear feature. Our findings provide a deeper comprehension of complex dynamic behaviors and contribute to the exploration of effective methods and strategies for controlling different states in a nonlinear cavity magnonic system.

I. INTRODUCTION

Cavity magnonic systems, as an interdisciplinary field of microwave photonics and magnetism, have attracted considerable attention in recent years due to their profound significance in fundamental physics and practical applications [1–29]. A microwave cavity can store electromagnetic energy and generate stable photon modes [30], while a magnon is the collective excitation of spins [31–33] in magnetic materials such as yttrium iron garnet (YIG) crystals with high spin density and ultralow damping [34]. The coupling between the two, via the magnetic dipole interaction, provides a unique research platform which not only helps to deepen the understanding of light-matter interactions but also has the potential to trigger technological innovations in the field of information technology. For example, coherent magnon-photon coupling facilitates robust information exchange between the processor and the carrier [5,35–37], and dissipative magnon-photon coupling enables unique properties such as nonreciprocal wave propagation [38] and slow light [39].

Although research on cavity magnonic systems has made rapid progress, most studies have focused on the linear range, and the exploration of nonlinear effects is still in its infancy. Nonlinear effects, as a ubiquitous phenomenon in nature, are of great significance in revealing the essential laws of nature. Different from the linear case under weak driving in which the system can be regarded as harmonic oscillators, anharmonic oscillators are excited and dominate the dynamic behavior of the system in the nonlinear case when it is subject to strong driving, leading to bistability with a hysteresis loop [40–42].

This is explained as the magnon Kerr effect caused by the magnetocrystalline anisotropy of the YIG crystal [40–43]. Intriguingly, the magnon Kerr effect can be positive or negative by adjusting the angle between the crystal axis and the external magnetic field [40], which not only enriches nonlinear behavior but also provides flexibility in device applications. Benefitting from the adjustability and expansibility of the cavity magnonic system, systems with different configurations exhibit other unique nonlinear characteristics based on the magnon Kerr effect. In non-Hermitian systems, the threshold of bistability is greatly reduced [44,45], and the sensitivity of the Kerr nonlinearity [46,47] and high-order sidebands [48] are significantly enhanced. When the system has two cavities, two YIG spheres, or a photon Kerr effect, nonreciprocal transmission [49] and multistability [50–52] can be achieved. For a system driven far from equilibrium, the Kerr nonlinear effect can entangle two magnon modes [53]. In addition, the saturation effect [54] or magnetostriction [55] of the YIG sphere can modulate the bistable characteristics of the system.

While nonlinear effects have been observed and characterized in these systems, deeply understanding nonlinear phenomena remains an important issue. In this paper, we carry out a theoretical study of state transfer in a nonlinear cavity magnonic system whose main physics is the photon and magnon Kerr effects. By setting different initial states, we record which coexisting state of the bistability or tristability they are eventually transferred to and explain state transfer based on the basins of attraction. Our results uncover the dependence of state transfer on the amplitude and phase of the magnon and photon.

The remainder of this paper is organized as follows. In Sec. II, we build the model of the nonlinear cavity magnonic system and derive the Heisenberg-Langevin equations of the operators and the higher-order nonlinear steady-state

*huawei.fan@xupt.edu.cn
†mingliang0301@163.com
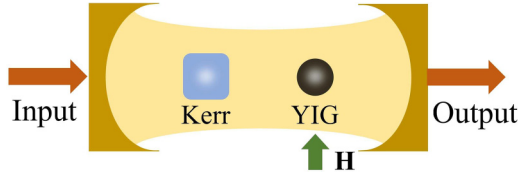
FIG. 1. Schematic layout of the cavity magnonic system, where a YIG sphere and a Kerr medium are placed in a microwave cavity. The cavity photon is driven by a microwave field via the input and output ports. The frequency of the Kittel mode is tuned by a uniform external magnetic field **H**.

equation of the magnon frequency shift. In Sec. III, applying the formulas derived in Sec. II, we demonstrate state transfer and explain it via the basins of attraction. Moreover, the influence of the photon and magnon Kerr effects on state transfer is also investigated in Sec. III. Finally, we summarize our findings in Sec. IV.

II. MODEL AND THEORY

The proposed system in our model is a YIG sphere coupled to a microwave cavity with a Kerr medium in it, as schematically shown in Fig. 1. A microwave field is injected from the input port and comes out from the output port to drive the cavity photon. In addition, a uniform external magnetic field **H** is applied to the YIG sphere to tune the frequency of the Kittel mode in which all spins precess uniformly.

Compared with the common cavity magnonic system [1,3–5,7], the total Hamiltonian in our model also needs to introduce the photon and magnon Kerr nonlinearities because of the Kerr medium in the cavity [54,56] and the magnetocrystalline anisotropy of the YIG sphere [40,43], and therefore, it can be written as

$$H/\hbar = \omega_c a^\dagger a + \omega_m m^\dagger m + K_a a^\dagger a a^\dagger a + K_m m^\dagger m m^\dagger m$$
$$+ g(a^\dagger m + a m^\dagger) + \Omega_d(a^\dagger e^{-i\omega_d t} + a e^{i\omega_d t}). \quad (1)$$

Here $a^\dagger$ and a ($m^\dagger$ and m) are the photon (magnon) creation and annihilation operators, respectively. The first two terms are the bare Hamiltonians of the photon and magnon with frequencies ω_c and ω_m, respectively. The next two terms describe the photon and magnon Kerr effects with Kerr coefficients K_a and K_m, respectively. The fifth term denotes the interaction between the photon and magnon with the coupling strength g. The last term represents the driving of the cavity photon with driving strength Ω_d and driving frequency ω_d. The driving strength Ω_d is related to the driving power P_d as $\Omega_d = \sqrt{P_d \kappa_{c1}/(\hbar \omega_d)}$, where κ_{c1} is the external damping rate of the photon due to the input port. In a frame rotating with ω_d, the Hamiltonian in Eq. (1) can be rewritten as

$$H/\hbar = \delta_c a^\dagger a + \delta_m m^\dagger m + K_a a^\dagger a a^\dagger a + K_m m^\dagger m m^\dagger m$$
$$+ g(a^\dagger m + a m^\dagger) + \Omega_d(a^\dagger + a), \quad (2)$$

where $\delta_c = \omega_c - \omega_d$ and $\delta_m = \omega_m - \omega_d$ are the frequency detunings of the photon and magnon relative to the driving frequency, respectively.

Using a quantum Langevin method [57] for Eq. (2), we can obtain the equations of motion of operators a and m:

$$\dot{a} = -i\left[\left(\delta_c - i\frac{\kappa_c}{2}\right)a + 2K_a a^\dagger a a + gm + \Omega_d\right],$$
$$\dot{m} = -i\left[\left(\delta_m - i\frac{\gamma_m}{2}\right)m + 2K_m m^\dagger m m + ga\right], \quad (3)$$

where κ_c and γ_m are the damping rates of the photon and magnon, respectively. We write operators a and m as the sum of expectation values and fluctuations, $a = \langle a \rangle + \delta a$ and $m = \langle m \rangle + \delta m$, then substitute them into Eq. (3), and, eventually, obtain the equations of motion for the expectation values $\langle a \rangle$ and $\langle m \rangle$:

$$\langle \dot{a} \rangle = -i\left[\left(\delta_c + \Delta_a - i\frac{\kappa_c}{2}\right)\langle a \rangle + g\langle m \rangle + \Omega_d\right],$$
$$\langle \dot{m} \rangle = -i\left[\left(\delta_m + \Delta_m - i\frac{\gamma_m}{2}\right)\langle m \rangle + g\langle a \rangle\right], \quad (4)$$

where $\Delta_a = 2K_a\langle a^\dagger \rangle\langle a \rangle = 2K_a|\langle a \rangle|^2$ and $\Delta_m = 2K_m\langle m^\dagger \rangle\langle m \rangle = 2K_m|\langle m \rangle|^2$ are the photon and magnon frequency shifts due to the photon and magnon Kerr effects, respectively. For a given Kerr coefficient, it can be seen that Δ_a and Δ_m are proportional to the excited photon and magnon numbers (i.e., $|\langle a \rangle|^2$ and $|\langle m \rangle|^2$), respectively. By solving Eq. (4) at the steady state, i.e., $\langle \dot{a} \rangle = 0$ and $\langle \dot{m} \rangle = 0$, we can obtain a higher-order nonlinear equation of Δ_m:

$$\left\{ \left\{ \delta_c + \frac{K_a\left[(\delta_m + \Delta_m)^2 + \frac{\gamma_m^2}{4}\right]\Delta_m}{K_m g^2} - \frac{g^2(\delta_m + \Delta_m)}{(\delta_m + \Delta_m)^2 + \frac{\gamma_m^2}{4}} \right\}^2 \right.$$
$$\left. + \left[\frac{\kappa_c}{2} + \frac{g^2\frac{\gamma_m}{2}}{(\delta_m + \Delta_m)^2 + \frac{\gamma_m^2}{4}}\right]^2 \right\}\left[(\delta_m + \Delta_m)^2 + \frac{\gamma_m^2}{4}\right]\Delta_m$$
$$- 2K_m\Omega_d^2 g^2 = 0. \quad (5)$$

Equations (4) and (5) are the main results of the theoretical derivation and the foundation for studying the nonlinear behavior in this paper.

III. RESULTS

In this section, the bistability and tristablity of the hybrid system with the coexisting states are shown by numerically solving Eq. (4) and analytically solving Eq. (5). By setting different initial states, state transfer in which the initial state evolves to the final state is presented. In order to explain state transfer and make the mechanism more transparent, a theoretical analysis is provided based on the basins of attraction. Furthermore, the influence of the photon and magnon Kerr effects on state transfer is investigated.

A. State transfer

When the system is under strong driving, the photon and magnon Kerr nonlinearities are triggered and jointly dominate the dynamics of the system. By using both numerical and analytical methods, we plot the magnon frequency shift $\Delta_m/2\pi$ versus the driving power P_d in Fig. 2. Here the numerical method is used to simulate the experiment by numerically solving Eq. (4), where P_d
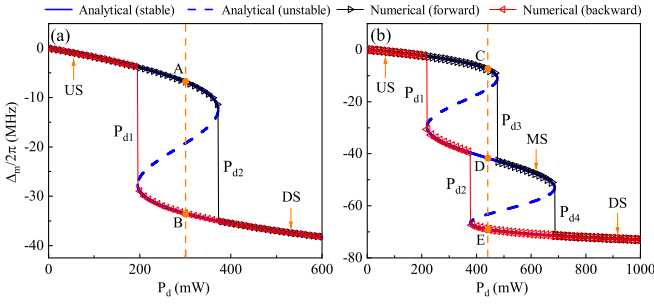
FIG. 2. Magnon frequency shifts $\Delta_m/2\pi$ versus the driving power P_d at (a) $\omega_d/2\pi = 10.044$ GHz and (b) $\omega_d/2\pi = 10.1227$ GHz. The black and red curves with triangles represent the numerically forward and backward sweeps of P_d, respectively. The blue solid and dashed lines denote the analytically stable and unstable states, respectively. The orange vertical dashed lines correspond to (a) $P_d = 300$ mW and (b) $P_d = 440$ mW.

adiabatically increases or decreases with a step $\delta P_d = 0.1$ mW. The parameters in our calculation are chosen to be $\omega_c/2\pi = 10.08$ GHz, $\omega_m/2\pi = 10.114$ GHz, $g/2\pi = 40$ MHz, $K_a/2\pi = 0.162$ nHz, $K_m/2\pi = -1.8$ nHz, $\kappa_c/2\pi = 4.5$ MHz, $\kappa_{c1}/2\pi = 3.0$ MHz, and $\gamma_m/2\pi = 12.5$ MHz.

Figure 2(a) shows the bistable behavior of the driving frequency $\omega_d/2\pi$ fixed at 10.044 GHz. Let US and DS denote the up and down stable states, respectively. When the driving power P_d is numerically swept forward (the black curve with triangles) from a value less than P_{d1} where the US is the only stable state, the system is in the basin of attraction of the US, which is why the observed stable state is the US. As P_d increases and passes through P_{d1}, the system is still in the basin of attraction of the US, until P_d increases to P_{d2}, where the basin of attraction of the US is absorbed by that of the DS. Then, a sharp switch from the US to DS occurs at P_{d2}, and the DS as the stable state substitutes for the US. For $P_d > P_{d2}$, the DS is the only stable state of the system. Similarly, when P_d is numerically swept backward (the red curve with triangles) from a value greater than P_{d2}, the system is located in the basin of attraction of the DS, and thus, the observed stable state is the DS until P_d decreases to P_{d1}. At P_{d1}, the basin of attraction of the DS is absorbed by that of the US, leading to a sharp switch from the DS to US, and then the US replaces the DS. For $P_d < P_{d1}$, the US is the only stable state of the system. By numerically sweeping P_d forward and backward, bistability with a clockwise hysteresis loop thus appears in the parameter interval $[P_{d1}, P_{d2}]$ in which the US and DS coexist. The analytical results (the blue curve) obtained with Eq. (5) are consistent with the numerical results, with the blue solid and dashed lines showing the analytically stable and unstable states, respectively.

Benefitting from the rich nonlinear physical mechanisms in this hybrid system, in addition to bistability in Fig. 2(a), tristability can also be achieved by tuning the driving frequency $\omega_d/2\pi$ to 10.1227 GHz. As shown in Fig. 2(b), there are two more sharp switches compared with the bistability. When sweeping the driving power P_d forward (the black curve with triangles) from a value less than P_{d1}, the numerically observable stable state is the US because the system is located
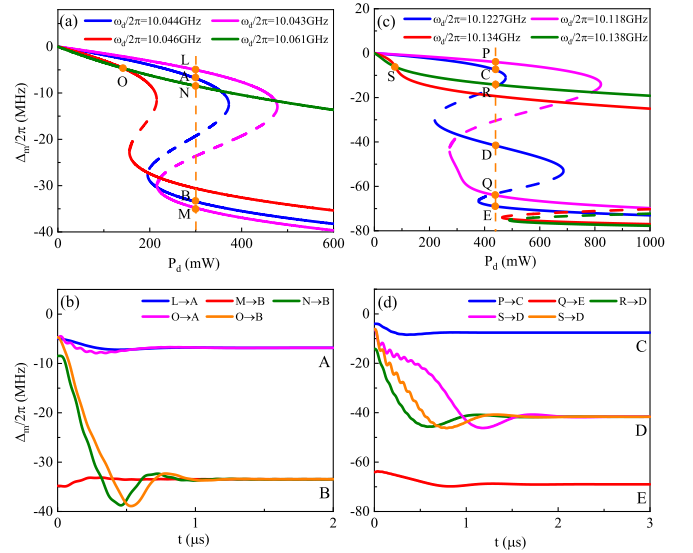
in the basin of attraction of the US until P_d reaches P_{d3}, at which point the basin of attraction of the US is absorbed by that of the middle stable state (MS), and thus, a sharp switch from the US to MS happens. When P_d increases to P_{d4}, another sharp switch from the MS to DS occurs as the basin of attraction of the MS is absorbed by that of the DS. For $P_d > P_{d4}$, the DS is the only stable state of the system. Likewise, when sweeping P_d backward (the red curve with triangles) from a value greater than P_{d4}, there are two sharp switches at P_{d2} (where the DS jumps to the MS) and P_{d1} (where the MS jumps to the US). For $P_d < P_{d1}$, the US is the only stable state of the system. The aforementioned numerical sweeping result leads to a more complex hysteresis loop compared with that of the bistability. The analytically stable states (the blue solid lines) obtained with Eq. (5) are consistent with the numerical results. The blue dashed lines are the analytically unstable states, which cannot be obtained with the numerical sweeping. Combining the numerical and analytical results, the tristable region in which the US, MS, and DS coexist is in the parameter interval $[P_{d2}, P_{d3}]$.

According to the characteristics of bistability and tristability, coexisting stable states in the bistable and tristable regions exist. If the system is at different initial states, which of the coexisting states will it eventually evolve to? We first study the bistable situation and choose points A and B [which are the coexisting states at $P_d = 300$ mW in Fig. 2(a)] as the final states. In experiments, the initial state cannot be freely modulated. Thus, we both utilize the stable state and adjust the system parameter to control the initial state. When the driving frequency $\omega_d/2\pi$ is tuned to be 10.043 GHz, we fix the initial state at points L and M, which are the stable states of the pink curve at $P_d = 300$ mW in Fig. 3(a). If we adjust $\omega_d/2\pi$ back to 10.044 GHz without changing P_d [where points A and B are the coexisting states of the blue curve in Fig. 3(a)], then

FIG. 3. (a) and (c) Magnon frequency shifts $\Delta_m/2\pi$ versus the driving power P_d for different values of the driving frequency $\omega_d/2\pi$. The orange vertical dashed lines correspond to (a) $P_d = 300$ mW and (c) $P_d = 440$ mW. (b) and (d) Time evolutions of $\Delta_m/2\pi$ from the different initial states to the final states.

points L and M evolve, respectively, to points A and B, as depicted by the blue and red curves in Fig. 3(b). It seems that if a point is close to point A (B), it should evolve to point A (B). However, that is not the case. For the initial state fixed at point N [the stable state of the green curve at $\omega_d/2\pi = 10.061$ GHz and $P_d = 300$ mW in Fig. 3(a)], although it is close to point A, it evolves to point B when $\omega_d/2\pi$ is adjusted back to 10.044 GHz, as described by the green curve in Fig. 3(b). Especially, when $\omega_d/2\pi$ is tuned to 10.046 GHz (the red curve) and 10.061 GHz (the green curve), a cross point O at $P_d = 143.4$ mW exists in Fig. 3(a). If we adjust $\omega_d/2\pi$ from 10.046 GHz back to 10.044 GHz and P_d from 143.4 mW back to 300 mW, then the system evolves from point O to A, as depicted by the pink curve in Fig. 3(b). However, when we adjust $\omega_d/2\pi$ from 10.061 GHz back to 10.044 GHz and P_d from 143.4 mW back to 300 mW, the system evolves from point O to B, as shown by the orange curve in Fig. 3(b). Therefore, for the same point O, it can evolve not only to point A but also to point B.

For the tristable situation, we choose points C, D, and E [which are the coexisting states at $P_d = 440$ mW in Fig. 2(b)] as the final states. We fix the initial state at points P and Q, which are the stable states of the pink curve at $\omega_d/2\pi = 10.118$ GHz and $P_d = 440$ mW in Fig. 3(c). When we adjust $\omega_d/2\pi$ back to 10.1227 GHz without changing P_d [where points C, D, and E are the coexisting states of the blue curve in Fig. 3(c)], then points P and Q evolve, respectively, to points C and E, as described by the blue and red curves in Fig. 3(d). When the initial state is fixed at point R, which is the stable state of the green curve at $\omega_d/2\pi = 10.138$ GHz and $P_d = 440$ mW in Fig. 3(c), although it is close to point C, it evolves to point D when $\omega_d/2\pi$ is adjusted back to 10.1227 GHz, as shown by the green curve in Fig. 3(d). For point S, which is the cross point of the red (corresponding to $\omega_d/2\pi = 10.134$ GHz) and green (corresponding to $\omega_d/2\pi = 10.138$ GHz) curves at $P_d = 75.84$ mW in Fig. 3(c), regardless of whether $\omega_d/2\pi$ is adjusted from 10.134 or 10.138 GHz back to 10.1227 GHz with P_d adjusted from 75.84 mW back to 440 mW, point S always evolves to point D, as depicted by the pink and orange curves in Fig. 3(d).

So far, we have presented the phenomenon of state transfer. The results show the following: (1) State transfer is sensitive to the initial state, for example, $L \rightarrow A$ and $N \rightarrow B$ in Fig. 3(b) and $P \rightarrow C$ and $R \rightarrow D$ in Fig. 3(d). (2) While state transfer is presented from the perspective of the number of excited magnons $|\langle m \rangle|^2$, it is not determined by only $|\langle m \rangle|^2$, for example, $O \rightarrow A$ and $O \rightarrow B$ in Fig. 3(b). (3) The dependence of state transfer on the initial state is highly nonlinear and complex.

B. Theoretical explanation

Next, we analyze the reason for the above state transfer. From the theoretical derivation, the evolution of the system is governed by Eq. (4), which is a differential equation in four-dimensional complex space, and the state vector is defined as $\Psi = (\langle a \rangle, \langle m \rangle) = [\text{Re}(\langle a \rangle), \text{Im}(\langle a \rangle), \text{Re}(\langle m \rangle), \text{Im}(\langle m \rangle)]$. Without changing the parameters of the system, the final state of the system depends only on the initial state of the system. For example,

TABLE I. State vectors corresponding to the points in Fig. 3(a). Ψ_{O_1} and Ψ_{O_2} represent the state vectors of point O at $\omega_d/2\pi = 10.046$ and 10.061 GHz, respectively. State vectors have been scaled down by 10^8.

Ψ	$\text{Re}(\langle a \rangle)$	$\text{Im}(\langle a \rangle)$	$\text{Re}(\langle m \rangle)$	$\text{Im}(\langle m \rangle)$
Ψ_A	-0.646	-0.245	0.390	0.194
Ψ_B	0.343	-0.825	-0.515	0.815
Ψ_L	-0.589	-0.188	0.343	0.146
Ψ_M	0.291	-0.855	-0.471	0.863
Ψ_N	0.493	-0.232	-0.463	0.144
Ψ_{O_1}	-0.520	-0.245	0.310	0.185
Ψ_{O_2}	0.394	-0.196	-0.341	0.119

in Fig. 2(a), the system starts from a specific initial state vector Ψ; then Ψ will reach state A or B (whose state vectors Ψ_A and Ψ_B are listed in Table I) in the bistable regime. In order to investigate the landscape of states A and B in the phase space of Ψ, the basins of attraction that are close to states A and B are shown in Fig. 4. In Fig. 4(a), we set the initial state vector of the system near state A and then observe the final state of the system. Since the basins of attraction are in four-dimensional complex space which cannot be directly presented, basins are present only in the two-dimensional complex plane. More specifically, we always
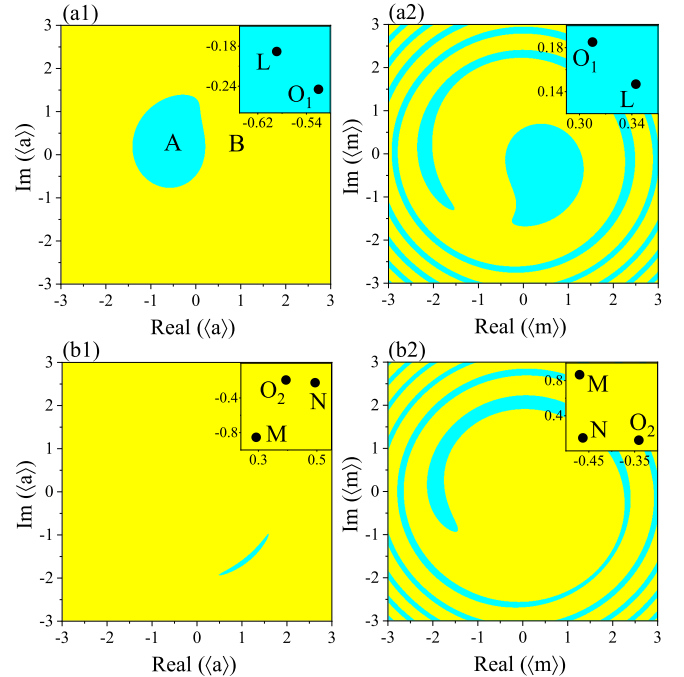
FIG. 4. Basins of attraction near states A and B. (a1) and (a2) correspond, respectively, to plane $[\text{Re}(\langle a \rangle), \text{Im}(\langle a \rangle)]$ for the initial value $\langle m \rangle$ fixed at $\langle m \rangle = (0.390, 0.194)$ and plane $[\text{Re}(\langle m \rangle), \text{Im}(\langle m \rangle)]$ for the initial value $\langle a \rangle$ fixed at $\langle a \rangle = (-0.646, -0.245)$ near state A. (b1) and (b2) correspond, respectively, to plane $[\text{Re}(\langle a \rangle), \text{Im}(\langle a \rangle)]$ for the initial value $\langle m \rangle$ fixed at $\langle m \rangle = (-0.515, 0.815)$ and plane $[\text{Re}(\langle m \rangle), \text{Im}(\langle m \rangle)]$ for the initial value $\langle a \rangle$ fixed at $\langle a \rangle = (0.343, -0.825)$ near state B. The cyan and yellow regions represent the initial state finally transferred to states A and B, respectively. The insets show an enlargement of the local area.

fix the initial value $\langle m \rangle$ at $\langle m \rangle = (0.390, 0.194)$ and pick up the initial value $\langle a \rangle$ in the phase space of $[\mathrm{Re}(\langle a \rangle), \mathrm{Im}(\langle a \rangle)]$ in Fig. 4(a1). After a long-term evolution, we record the final state of the system. The initial values are shown in cyan (yellow) if the system is finally transferred to state A (B). It can be seen that a smaller region A is surrounded by a larger region B in Fig. 4(a1), which means that although the initial state is near state A, it can be transferred to state B in addition to state A. In the vicinity of the boundary between two regions, a slight change in the initial value $\langle a \rangle$ can cause the system to reach different stable states. From the perspective of plane $[\mathrm{Re}(\langle m \rangle), \mathrm{Im}(\langle m \rangle)]$ when the initial value $\langle a \rangle$ is fixed at $\langle a \rangle = (-0.646, -0.245)$, there are two parts of region A: one displays a patchy distribution located at the middle; the other displays a spiral distribution around the middle, as shown in Fig. 4(a2). This spiral distribution creates more boundaries at larger initial values $|\langle m \rangle|$, which causes the final state to alternate between states A and B. When the initial state vector is fixed near state B, region A is very small in plane $[\mathrm{Re}(\langle a \rangle), \mathrm{Im}(\langle a \rangle)]$ for the initial value $\langle m \rangle$ fixed at $\langle m \rangle = (-0.515, 0.815)$, as shown in Fig. 4(b1), which means that the vast majority of the initial value $\langle a \rangle$ is finally transferred to state B. However, the spiral distribution of region A increases the probability of the transfer to state A at larger initial values $|\langle m \rangle|$ in plane $[\mathrm{Re}(\langle m \rangle), \mathrm{Im}(\langle m \rangle)]$ for the initial value $\langle a \rangle$ fixed at $\langle a \rangle = (0.343, -0.825)$, as shown in Fig. 4(b2). In addition, Fig. 4 shows that plane $[\mathrm{Re}(\langle m \rangle), \mathrm{Im}(\langle m \rangle)]$ exhibits an alternating pattern between states A and B at larger initial values $\langle m \rangle$, but plane $[\mathrm{Re}(\langle a \rangle), \mathrm{Im}(\langle a \rangle)]$ does not exhibit this phenomenon.

For adjacent state vectors, the dynamic properties of the system in phase space are similar. Therefore, we can use Fig. 4 to approximately explain state transfer in Fig. 3(b). If a state vector is close to state A (B), we use the basins of attraction near state A (B) to explain its transfer. As analyzed above, the state vector $\mathbf{\Psi}$ of each point is related to both the values $\langle a \rangle$ and $\langle m \rangle$; thus, we should not directly evaluate the distance between two states according to the intuitive distance, determined by the number of excited magnons $|\langle m \rangle|^2$, between two points in Fig. 3(a). To evaluate it more reasonably, we define $d_{ji} = |\langle a \rangle_j - \langle a \rangle_i| + |\langle m \rangle_j - \langle m \rangle_i|$ as the distance between state vectors $\mathbf{\Psi}_j$ and $\mathbf{\Psi}_i$, which includes the contributions from both values $\langle a \rangle$ and $\langle m \rangle$. Table I lists the state vectors of each point in Fig. 3(a), where $\mathbf{\Psi}_{O_1}$ and $\mathbf{\Psi}_{O_2}$ represent the state vectors of point O at $\omega_d/2\pi = 10.046$ and 10.061 GHz, respectively. Table I shows that although point O is the cross point in Fig. 3(a), it has different state vectors when the parameters are different. With the calculation of d_{jA} and d_{jB} ($j = L, M, N, O_1$, and O_2), state L is close to state A as $d_{LA} = 0.148 < d_{LB} = 2.217$, and states M and N are close to state B as $d_{MB} = 0.125 < d_{MA} = 2.208$ and $d_{NB} = 1.285 < d_{NA} = 1.993$. This is not exactly the same as the intuitive distance in Fig. 3(a). To explain state transfer in Fig. 3(b), we approximately mark the position of state L in the insets of Figs. 4(a1) and 4(a2), where we consider only the value $\langle a \rangle$ of state L in plane $[\mathrm{Re}(\langle a \rangle), \mathrm{Im}(\langle a \rangle)]$ and the value $\langle m \rangle$ of state L in plane $[\mathrm{Re}(\langle m \rangle), \mathrm{Im}(\langle m \rangle)]$. Since state L falls into region A, it is eventually transferred to state A. Similarly, we approximately mark the positions of states M and N in the insets of Figs. 4(b1) and 4(b2), which fall into

TABLE II. State vectors corresponding to the points in Fig. 3(c). $\mathbf{\Psi}_{S_1}$ and $\mathbf{\Psi}_{S_2}$ represent the state vectors of point S at $\omega_d/2\pi = 10.134$ and 10.138 GHz, respectively. State vectors have been scaled down by 10^8.

$\mathbf{\Psi}$	$\mathrm{Re}(\langle a \rangle)$	$\mathrm{Im}(\langle a \rangle)$	$\mathrm{Re}(\langle m \rangle)$	$\mathrm{Im}(\langle m \rangle)$
$\mathbf{\Psi}_C$	-0.155	-0.126	-0.436	-0.143
$\mathbf{\Psi}_D$	0.898	-1.026	0.603	-0.890
$\mathbf{\Psi}_E$	-0.880	-2.550	-0.555	-1.268
$\mathbf{\Psi}_P$	-0.055	-0.064	-0.327	-0.064
$\mathbf{\Psi}_Q$	-0.995	-2.049	-0.690	-1.141
$\mathbf{\Psi}_R$	0.530	-0.296	0.491	-0.391
$\mathbf{\Psi}_{S_1}$	-0.069	-0.269	-0.193	-0.366
$\mathbf{\Psi}_{S_2}$	0.149	-0.281	0.116	-0.397

region B and thus are eventually transferred to state B. Interestingly, state O_1 is close to state A at $\omega_d/2\pi = 10.046$ GHz as $d_{O_1A} = 0.207 < d_{O_1B} = 2.079$ and is eventually transferred to state A as it falls into region A in the insets of Figs. 4(a1) and 4(a2). But state O_2 is close to state B at $\omega_d/2\pi = 10.061$ GHz as $d_{O_2B} = 1.348 < d_{O_2A} = 1.776$ and is eventually transferred to state B as it falls into region B in the insets of Figs. 4(b1) and 4(b2).

In the tristable regime, we plot the basins of attraction near states C, D, and E (whose state vectors $\mathbf{\Psi}_C$, $\mathbf{\Psi}_D$, and $\mathbf{\Psi}_E$ are listed in Table II) to study their landscape in the phase space of $\mathbf{\Psi}$. As shown in Fig. 5, the cyan, pink, and yellow regions represent the initial values finally transferred to states C, D, and E, respectively. In plane $[\mathrm{Re}(\langle a \rangle), \mathrm{Im}(\langle a \rangle)]$, regions C and E display the spiral distributions, with region D filled with the remaining space, as shown in Figs. 5(a1), 5(b1), and 5(c1), which makes the final states alternate among states C, D, and E at larger initial values $|\langle a \rangle|$. This is contrary to Figs. 4(a2) and 4(b2), where the alternation occurs in plane $[\mathrm{Re}(\langle m \rangle), \mathrm{Im}(\langle m \rangle)]$ at larger initial values $|\langle m \rangle|$. In addition, there is a region C in the middle of Fig. 5(a1). In plane $[\mathrm{Re}(\langle m \rangle), \mathrm{Im}(\langle m \rangle)]$, however, region C (E) is surrounded by region D, but there is no region E (C), as shown in Fig. 5(a2) [Fig. 5(c2)]. This means that the system can be transferred only to states C (E) and D without state E (C). In Fig. 5(b2), only region D exists, causing the system to be transferred only to state D without states C and E. The white regions are invalid in Figs. 5(a2), 5(b2), and 5(c2), where the system evolves to infinity.

Table II lists the state vectors of each point in Fig. 3(c), where $\mathbf{\Psi}_{S_1}$ and $\mathbf{\Psi}_{S_2}$ represent the state vectors of point S at $\omega_d/2\pi = 10.134$ and 10.138 GHz, respectively. According to the definition of the distance between two states, we calculate d_{jC}, d_{jD}, and d_{jE} ($j = P, Q, R, S_1$, and S_2). States P, R, and Q are, respectively, close to states C, D, and E as $d_{PC} = 0.253 < d_{PD} = 2.598 < d_{PE} = 3.844$, $d_{RD} = 1.329 < d_{RC} = 1.665 < d_{RE} = 4.024$, and $d_{QE} = 0.699 < d_{QC} = 3.128 < d_{QD} = 3.469$. By approximately marking the positions of states C, D, and E in the basins of attraction, we find that states P, R, and Q fall, respectively, into regions C, D, and E in the insets of Fig. 5, which explains why states P, R, and Q were, respectively, transferred to states C, D, and E in Fig. 3(d). Both states S_1 and S_2 are close to state C as $d_{S_1C} = 0.497 < d_{S_1D} = 2.181 < d_{S_1E} = 3.393$ and d_{S_2C}
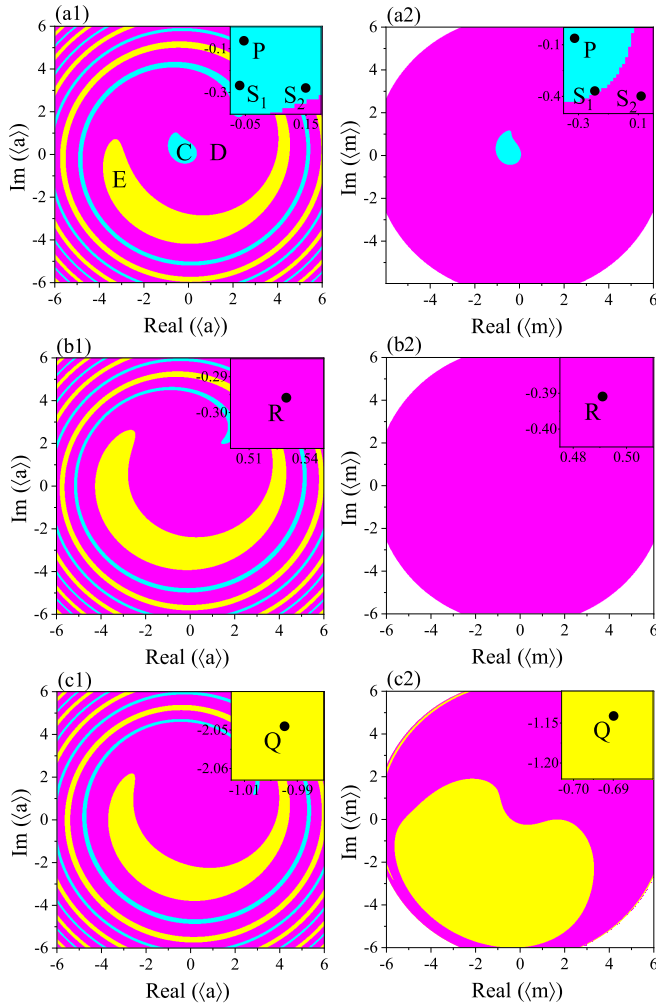
FIG. 5. Basins of attraction near states C, D, and E. (a1) and (a2) correspond, respectively, to plane [Re($\langle a \rangle$), Im($\langle a \rangle$)] for the initial value $\langle m \rangle$ fixed at $\langle m \rangle = (-0.436, -0.143)$ and plane [Re($\langle m \rangle$), Im($\langle m \rangle$)] for the initial value $\langle a \rangle$ fixed at $\langle a \rangle = (-0.155, -0.126)$ near state C. (b1) and (b2) correspond, respectively, to plane [Re($\langle a \rangle$), Im($\langle a \rangle$)] for the initial value $\langle m \rangle$ fixed at $\langle m \rangle = (0.603, -0.890)$ and plane [Re($\langle m \rangle$), Im($\langle m \rangle$)] for the initial value $\langle a \rangle$ fixed at $\langle a \rangle = (0.898, -1.026)$ near state D. (c1) and (c2) correspond, respectively, to plane [Re($\langle a \rangle$), Im($\langle a \rangle$)] for the initial value $\langle m \rangle$ fixed at $\langle m \rangle = (-0.555, -1.268)$ and plane [Re($\langle m \rangle$), Im($\langle m \rangle$)] for the initial value $\langle a \rangle$ fixed at $\langle a \rangle = (-0.880, -2.550)$ near state E. The cyan, pink, and yellow regions represent the initial values finally transferred to states C, D, and E, respectively. The white regions are invalid, where the system evolves to infinity. The insets show an enlargement of the local area.

$= 0.949 < d_{S_2D} = 1.749 < d_{S_2E} = 3.590$. From Fig. 3(d), regardless of whether the driving frequency $\omega_d/2\pi$ is 10.134 or 10.138 GHz, state S always evolves to state D. Thus, states S_1 and S_2 should fall into region D in the insets of Figs. 5(a1) and 5(a2). However, only state S_2 falls into region D in plane [Re($\langle m \rangle$), Im($\langle m \rangle$)], and others fall into region C. This is because states S_1 and S_2 located near the boundary between regions C and D are sensitive to the boundary, whose state transfer cannot be approximately explained by the insets of Figs. 5(a1) and 5(a2).

C. Influence of the photon and magnon Kerr effects on state transfer

As studied above, the basin of attraction effectively describes state transfer. In our model, however, the photon and magnon Kerr effects may play distinct roles in the basin of attraction, thereby influencing the characteristics of state transfer. For this reason, we show the basins of attraction when the photon and magnon Kerr effects separately dominate the nonlinear dynamics of the system. For $\omega_m/2\pi = 9.7$ GHz, where the photon and magnon are far off resonance, the upper polariton mode, due to the interaction between the subsystems, mainly contains the photon component. Therefore, as the driving frequency $\omega_d/2\pi = 10.095$ GHz approaches the upper polariton mode, only the photon Kerr effect is excited and contributes to nonlinearity, resulting in the manifestation of bistability depicted in Fig. 6(a). We choose coexisting states F and G at $P_d = 150$ mW as an example. According to state vectors $\mathbf{\Psi}_F = (0.644, -0.157, 0.065, -0.017)$ and $\mathbf{\Psi}_G = (-1.404, -1.450, -0.144, -0.144)$, we calculate, respectively, the photon and magnon Kerr energies, $\Xi_a^{FG}/h = (K_a/2\pi)(|\langle a_F \rangle|^4 + |\langle a_G \rangle|^4) = 27.197$ MHz and $\Xi_m^{FG}/h = (|K_m|/2\pi)(|\langle m_F \rangle|^4 + |\langle m_G \rangle|^4) = 0.031$ MHz, which further confirms the dominance of the photon Kerr effect due to $\Xi_a^{FG}/h \gg \Xi_m^{FG}/h$. By plotting the basins of attraction near the coexisting states, regions F and G exhibit a spiral distribution in plane [Re($\langle a \rangle$), Im($\langle a \rangle$)], as shown in Figs. 6(b1) and 6(c1). However, in plane [Re($\langle m \rangle$), Im($\langle m \rangle$)], only a single region F or G exists, as depicted in Figs. 6(b2) and 6(c2). These results indicate that when the photon Kerr effect dominates, adjusting the initial value $\langle a \rangle$ can effectively achieve different state transfers because the spiral distribution causes different regions to alternate. For $\omega_m/2\pi = 10.25$ GHz and $\omega_d/2\pi = 10.247$ GHz, only the magnon Kerr effect is excited and contributes to nonlinearity since in this case, the upper polariton mode, which mainly contains the magnon component, is driven. The nonlinear behavior of the system also displays bistability, as shown in Fig. 7(a). We choose coexisting states H [$\mathbf{\Psi}_H = (0.023, -0.055, -0.286, -0.230)$] and K [$\mathbf{\Psi}_K = (0.072, -0.137, -0.076, -0.568)$] at $P_d = 850$ mW (where $\Xi_m^{HK}/h = 2.268$ MHz $\gg \Xi_a^{HK}/h = 0.001$ MHz, indicating that the magnon Kerr effect dominates the nonlinear dynamics of the system) and plot the basins of attraction near them in Figs. 7(b1)–7(c2). State transfer exhibits a spiral distribution in plane [Re($\langle m \rangle$), Im($\langle m \rangle$)] in Figs. 7(b2) and 7(c2), but it displays a patchy distribution in plane [Re($\langle a \rangle$), Im($\langle a \rangle$)] in Figs. 7(b1) and 7(c1), the opposite of the situation with photon Kerr effect.

When both the photon and magnon Kerr effects contribute to nonlinear dynamics, the distribution characteristics of state transfer in the basins of attraction depend on the photon and magnon Kerr effects. We take Fig. 2(a) as an example of where the system also shows bistability, and the magnon Kerr effect is stronger than the photon Kerr effect (i.e., $\Xi_m^{AB}/h = 16.198$ MHz $> \Xi_a^{AB}/h = 1.401$ MHz). State transfer displays a spiral distribution in plane [Re($\langle m \rangle$), Im($\langle m \rangle$)], but it appears trivially in plane [Re($\langle a \rangle$), Im($\langle a \rangle$)], as shown in Fig. 4.

Before ending this section, we would like to mention that compared to the focus of previous studies on the nonlinear
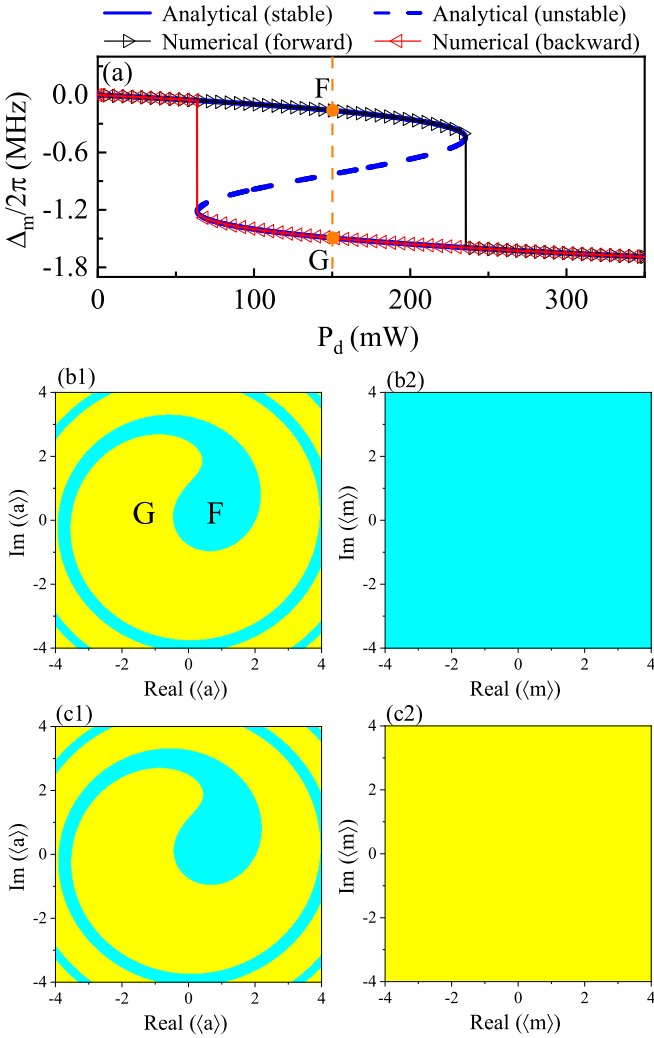
FIG. 6. (a) Bistability dominated by the photon Kerr effect when $\omega_m/2\pi = 9.7$ GHz and $\omega_d/2\pi = 10.095$ GHz. The orange vertical dashed line corresponds to $P_d = 150$ mW. (b1) and (b2) are the basins of attraction near state F, corresponding, respectively, to plane $[\text{Re}(\langle a \rangle), \text{Im}(\langle a \rangle)]$ for the initial value $\langle m \rangle$ fixed at $\langle m \rangle = (0.065, -0.017)$ and plane $[\text{Re}(\langle m \rangle), \text{Im}(\langle m \rangle)]$ for the initial value $\langle a \rangle$ fixed at $\langle a \rangle = (0.644, -0.157)$. (c1) and (c2) are the basins of attraction near state G, corresponding, respectively, to plane $[\text{Re}(\langle a \rangle), \text{Im}(\langle a \rangle)]$ for the initial value $\langle m \rangle$ fixed at $\langle m \rangle = (-0.144, -0.144)$ and plane $[\text{Re}(\langle m \rangle), \text{Im}(\langle m \rangle)]$ for the initial value $\langle a \rangle$ fixed at $\langle a \rangle = (-1.404, -1.450)$. The cyan and yellow regions represent the initial state finally transferred to states F and G, respectively.

FIG. 7. (a) Bistability dominated by the magnon Kerr effect when $\omega_m/2\pi = 10.25$ GHz and $\omega_d/2\pi = 10.247$ GHz. The orange vertical dashed line corresponds to $P_d = 850$ mW. (b1) and (b2) are the basins of attraction near state H, corresponding, respectively, to plane $[\text{Re}(\langle a \rangle), \text{Im}(\langle a \rangle)]$ for the initial value $\langle m \rangle$ fixed at $\langle m \rangle = (-0.286, -0.230)$ and plane $[\text{Re}(\langle m \rangle), \text{Im}(\langle m \rangle)]$ for the initial value $\langle a \rangle$ fixed at $\langle a \rangle = (0.023, -0.055)$. (c1) and (c2) are the basins of attraction near state K, corresponding, respectively, to plane $[\text{Re}(\langle a \rangle), \text{Im}(\langle a \rangle)]$ for the initial value $\langle m \rangle$ fixed at $\langle m \rangle = (-0.076, -0.568)$ and plane $[\text{Re}(\langle m \rangle), \text{Im}(\langle m \rangle)]$ for the initial value $\langle a \rangle$ fixed at $\langle a \rangle = (0.072, -0.137)$. The cyan and yellow regions represent the initial state finally transferred to states H and K, respectively.

dynamics of the same Hamiltonian as in Eq. (1) [58–61], state transfer goes further based on bistability and multistability and offers deeper insight into the intricate nonlinear dynamics of the system. In general, coexisting states exist in bistability or multistability, and each of them carries distinct physical meanings and practical applications. Hence, for a given initial state, it is very necessary to study which state it will finally transfer to because this knowledge is pivotal for predicting and controlling the nonlinear behaviors in experiments and applications.

IV. SUMMARY

To summarize, we have studied state transfer in a nonlinear cavity magnonic system with the photon and magnon Kerr effects involved. From the perspective of the number of excited magnons, the magnon frequency shift exhibited bistability and tristability, where the coexisting states lived, as a function of the driving power via appropriate adjustment of the parameters. Different initial states were eventually transferred to the same or different coexisting states of bistability and tristability. While state transfer was presented from the

perspective of the number of excited magnons, the ultimate transfer to a particular coexisting state was not determined only by the number of excited magnons. Investigating the basins of attraction, we found that state transfer was jointly dominated by the amplitude and phase of the magnon and photon. Moreover, the main characteristics of state transfer depend on the Kerr effects. Our findings offer comprehensive insight into nonlinear dynamics while also serving as a directive for nonlinear control strategies grounded in cavity magnonic systems.

[1] Ö. O. Soykal and M. E. Flatté, Phys. Rev. Lett. **104**, 077202 (2010).

[2] Ö. O. Soykal and M. E. Flatté, Phys. Rev. B **82**, 104413 (2010).

[3] H. Huebl, C. W. Zollitsch, J. Lotze, F. Hocke, M. Greifenstein, A. Marx, R. Gross, and S. T. B. Goennenwein, Phys. Rev. Lett. **111**, 127003 (2013).

[4] Y. Tabuchi, S. Ishino, T. Ishikawa, R. Yamazaki, K. Usami, and Y. Nakamura, Phys. Rev. Lett. **113**, 083603 (2014).

[5] X. Zhang, C.-L. Zou, L. Jiang, and H. X. Tang, Phys. Rev. Lett. **113**, 156401 (2014).

[6] M. Goryachev, W. G. Farr, D. L. Creedon, Y. Fan, M. Kostylev, and M. E. Tobar, Phys. Rev. Appl. **2**, 054002 (2014).

[7] D. Zhang, X.-M. Wang, T.-F. Li, X.-Q. Luo, W. Wu, F. Nori, and J. You, npj Quantum Inf. **1**, 15014 (2015).

[8] Y. Cao, P. Yan, H. Huebl, S. T. B. Goennenwein, and G. E. W. Bauer, Phys. Rev. B **91**, 094423 (2015).

[9] B. Zare Rameshti, Y. Cao, and G. E. W. Bauer, Phys. Rev. B **91**, 214430 (2015).

[10] L. Bai, M. Harder, Y. P. Chen, X. Fan, J. Q. Xiao, and C.-M. Hu, Phys. Rev. Lett. **114**, 227201 (2015).

[11] X. Zhang, C.-L. Zou, L. Jiang, and H. X. Tang, Sci. Adv. **2**, e1501286 (2016).

[12] D. Zhang, X.-Q. Luo, Y.-P. Wang, T.-F. Li, and J. Q. You, Nat. Commun. **8**, 1368 (2017).

[13] B. Zare Rameshti and G. E. W. Bauer, Phys. Rev. B **97**, 014419 (2018).

[14] Y. Li, T. Polakovic, Y.-L. Wang, J. Xu, S. Lendinez, Z. Zhang, J. Ding, T. Khaire, H. Saglam, R. Divan, J. Pearson, W.-K. Kwok, Z. Xiao, V. Novosad, A. Hoffmann, and W. Zhang, Phys. Rev. Lett. **123**, 107701 (2019).

[15] J. T. Hou and L. Liu, Phys. Rev. Lett. **123**, 107702 (2019).

[16] H. Y. Yuan, P. Yan, S. Zheng, Q. Y. He, K. Xia, and M.-H. Yung, Phys. Rev. Lett. **124**, 053602 (2020).

[17] J. Xu, C. Zhong, X. Han, D. Jin, L. Jiang, and X. Zhang, Phys. Rev. Lett. **125**, 237201 (2020).

[18] B. Yao, Y. S. Gui, J. W. Rao, Y. H. Zhang, W. Lu, and C.-M. Hu, Phys. Rev. Lett. **130**, 146702 (2023).

[19] D. Xu, X.-K. Gu, H.-K. Li, Y.-C. Weng, Y.-P. Wang, J. Li, H. Wang, S.-Y. Zhu, and J. Q. You, Phys. Rev. Lett. **130**, 193603 (2023).

[20] M. Harder, Y. Yang, B. M. Yao, C. H. Yu, J. W. Rao, Y. S. Gui, R. L. Stamps, and C.-M. Hu, Phys. Rev. Lett. **121**, 137203 (2018).

[21] V. L. Grigoryan, K. Shen, and K. Xia, Phys. Rev. B **98**, 024406 (2018).

[22] B. Bhoi, B. Kim, S.-H. Jang, J. Kim, J. Yang, Y.-J. Cho, and S.-K. Kim, Phys. Rev. B **99**, 134426 (2019).

[23] P.-C. Xu, J. W. Rao, Y. S. Gui, X. Jin, and C.-M. Hu, Phys. Rev. B **100**, 094415 (2019).

[24] W. Yu, J. Wang, H. Y. Yuan, and J. Xiao, Phys. Rev. Lett. **123**, 227201 (2019).

[25] Y. Yang, J. W. Rao, Y. S. Gui, B. M. Yao, W. Lu, and C.-M. Hu, Phys. Rev. Appl. **11**, 054023 (2019).

[26] G. Zhao, Y. Wang, and X.-F. Qian, Phys. Rev. B **104**, 134423 (2021).

[27] J. M. P. Nair, D. Mukhopadhyay, and G. S. Agarwal, Phys. Rev. B **105**, 214418 (2022).

[28] G.-Q. Zhang, W. Feng, W. Xiong, Q.-P. Su, and C.-P. Yang, Phys. Rev. A **107**, 012410 (2023).

[29] Y. Yang, Y. Xiao, and C.-M. Hu, Phys. Rev. B **107**, 054413 (2023).

[30] D. M. Pozar, *Microwave Engineering* (Wiley, New York, 2011).

[31] F. Bloch, Z. Phys. **61**, 206 (1930).

[32] T. Holstein and H. Primakoff, Phys. Rev. **58**, 1098 (1940).

[33] F. J. Dyson, Phys. Rev. **102**, 1217 (1956).

[34] M. Wu and A. Hoffmann, in *Recent Advances in Magnetic Insulators—From Spintronics to Microwave Applications*, edited by M. Wu and A. Hoffmann, Solid State Physics Vol. 64 (Academic Press, Cambridge, MA, 2013), pp. 1–392.

[35] X. Zhang, C.-L. Zou, N. Zhu, F. Marquardt, L. Jiang, and H. X. Tang, Nat. Commun. **6**, 8914 (2015).

[36] Y. Tabuchi, S. Ishino, A. Noguchi, T. Ishikawa, R. Yamazaki, K. Usami, and Y. Nakamura, Science **349**, 405 (2015).

[37] I. Boventer, C. Dörflinger, T. Wolz, R. Macêdo, R. Lebrun, M. Kläui, and M. Weides, Phys. Rev. Res. **2**, 013154 (2020).

[38] Y.-P. Wang, J. W. Rao, Y. Yang, P.-C. Xu, Y. S. Gui, B. M. Yao, J. Q. You, and C.-M. Hu, Phys. Rev. Lett. **123**, 127202 (2019).

[39] Y. Yang, Y.-P. Wang, J. W. Rao, Y. S. Gui, B. M. Yao, W. Lu, and C.-M. Hu, Phys. Rev. Lett. **125**, 147202 (2020).

[40] Y.-P. Wang, G.-Q. Zhang, D. Zhang, T.-F. Li, C.-M. Hu, and J. Q. You, Phys. Rev. Lett. **120**, 057202 (2018).

[41] P. Hyde, B. M. Yao, Y. S. Gui, G.-Q. Zhang, J. Q. You, and C.-M. Hu, Phys. Rev. B **98**, 174423 (2018).

[42] G. Zhang, Y. Wang, and J. You, Sci. China: Phys., Mech. Astron. **62**, 987511 (2019).

[43] Y.-P. Wang, G.-Q. Zhang, D. Zhang, X.-Q. Luo, W. Xiong, S.-P. Wang, T.-F. Li, C.-M. Hu, and J. Q. You, Phys. Rev. B **94**, 224410 (2016).

[44] J. M. P. Nair, D. Mukhopadhyay, and G. S. Agarwal, Phys. Rev. B **103**, 224401 (2021).

[45] H. Pan, Y. Yang, Z. H. An, and C.-M. Hu, Phys. Rev. B **106**, 054425 (2022).

[46] J. M. P. Nair, D. Mukhopadhyay, and G. S. Agarwal, Phys. Rev. Lett. **126**, 180401 (2021).

[47] G.-Q. Zhang, Y. Wang, and W. Xiong, Phys. Rev. B **107**, 064417 (2023).

[48] C. Zhao, Z. Yang, R. Peng, J. Yang, C. Li, and L. Zhou, Phys. Rev. Appl. **18**, 044074 (2022).

[49] C. Kong, H. Xiong, and Y. Wu, Phys. Rev. Appl. **12**, 034001 (2019).

[50] J. M. P. Nair, Z. Zhang, M. O. Scully, and G. S. Agarwal, Phys. Rev. B **102**, 104415 (2020).

[51] R.-C. Shen, Y.-P. Wang, J. Li, S.-Y. Zhu, G. S. Agarwal, and J. Q. You, Phys. Rev. Lett. **127**, 183202 (2021).

[52] M.-X. Bi, H. Fan, X.-H. Yan, and Y.-C. Lai, Phys. Rev. Lett. **132**, 137201 (2024).

[53] Z. Zhang, M. O. Scully, and G. S. Agarwal, Phys. Rev. Res. **1**, 023021 (2019).

[54] M. X. Bi, X. H. Yan, Y. Zhang, and Y. Xiao, Phys. Rev. B **103**, 104411 (2021).

[55] R.-C. Shen, J. Li, Z.-Y. Fan, Y.-P. Wang, and J. Q. You, Phys. Rev. Lett. **129**, 123601 (2022).

[56] P. D. Drummond and D. F. Walls, J. Phys. A **13**, 725 (1980).

[57] D. F. Walls and G. J. Milburn, *Quantum Optics* (Springer, Berlin, 1994).

[58] B. Y. Nikitchuk, E. V. Anikin, N. S. Maslova, and N. A. Gippius, Sci. Rep. **13**, 2997 (2023).

[59] D. Stefanatos and E. Paspalakis, Phys. Rev. A **102**, 013716 (2020).

[60] S. R. K. Rodriguez, V. Goblot, N. C. Zambon, A. Amo, and J. Bloch, Phys. Rev. A **99**, 013851 (2019).

[61] X.-W. Xu and Y. Li, Phys. Rev. A **90**, 033809 (2014).